Materials Characterization 223 (2025) 114859

Contents lists available at ScienceDirect

Materials Characterization

journal homepage: www.elsevier.com/locate/matchar

Novel texture analysis method for optimising material property in extruded 6xxx alloys using artificial neural networks

Mian Zhou [a,*], Chrysoula Tzileroglou [b], Carla Barbatti [b,c], Hamid Assadi [a]

[a] Brunel University London, UK
[b] Constellium University Technology Centre, Brunel University London, Uxbridge, UK
[c] Constellium Technology Center (C-TEC), Voreppe, France

ARTICLE INFO

Keywords:
Crystallographic texture
Aluminium
Extrusion
Finite element analysis
Artificial neural networks

ABSTRACT

This study investigates the extruded texture of a 6xxx series high-strength aluminium alloy as a function of profile geometry using Electron Backscatter Diffraction (EBSD) and X-Ray diffraction pattern (XRD). A novel texture analysis method was designed to acquire and prepare reliable texture data for machine learning applications. The method categorizes textures into five distinct groups, with volume fractions calculated for each group. Furthermore, finite element analysis of the extrusion process revealed that axial tensile strain promotes a combination of ⟨100⟩ and ⟨111⟩ //ED texture components, while shear deformation induces ⟨211⟩ //ED texture components. The results were subsequently fed into an artificial neural network (ANN) model developed to link the texture to profile geometry, which governs the deformation modes experienced during the material flow. This approach represents a significant advancement towards real-time control of material properties during extrusion.

1. Introduction

Aluminium alloys are increasingly used in the automotive sector for their lightweight properties, offering up to a 28 % reduction in vehicle weight compared to steel [1], which significantly lowers CO2 emissions and improves fuel efficiency. Aluminium alloys of 6xxx are particularly valued for their corrosion resistance, weldability, formability and recyclability [2,3]. Extrusion, one of the oldest and most complex manufacturing technologies, is the main processing method for wrought aluminium alloys. Higher performance and more complex-shaped extruded aluminium components are increasingly demanded by the industry to meet decarbonization targets. A comprehensive understanding of the process-microstructure-property relationship is essential to enhance product performance [4]. While much research has been conducted on texture development in rolled aluminium alloys [5– 6], the texture evolution in extruded 6xxx aluminium alloys remains less understood. Most research [7– 12] has investigated small-scale laboratory extrusions, mainly focusing on round bar profiles, for which a combined <100> and < 111> duplex fibre has been widely reported. Zhang et.al [10] studied the texture variation of an Al-Si-Mg round bar extruded at 300 °C (lower than temperatures that may be typically applied in the industrial practice for this type of alloy) and reported the duplex fibre texture is strongest in the centre region and becomes weaker and rotated when approaching the surface. Studying the deformation texture of extruded flat profile, Furu and Vatne [12] observed a strong β fibre and Cube texture component at the centre, weak to nearly random texture at the surface. The β fibre extends from the Brass component{110}⟨112⟩ to the Copper component {112} < 111>, with the S orientations (S1 component {124} ⟨211⟩, S2 component of {124} < 412>, and S3 component of {123} < 634>) located at the intermediate position along the fibre. These findings indicate the presence of typical copper-type texture along with Cube components in extruded flat profiles, as copper-type rolling texture in FCC metals is generally described by the superposition of Copper, S and Brass components.

In contrast to the plane strain deformation in rolling, aluminium experiences more severe plastic deformation at higher temperatures (typically above 500 °C) and follows complex deformation paths during extrusion. Finite element (FE) modelling is extensively used to investigate the extrusion process where interactions between the die, billet and container at high temperatures, combined with intricate die geometry significantly influence the material flow [13]. Various research has used FE modelling to simulate extruded texture, commonly simplified the extrusion deformation to a 2D model [14].

Machine learning (ML) has seen rapid adoption in material

* Corresponding author.
E-mail addresses: mian.zhou2@brunel.ac.uk (M. Zhou), chrysoula.tzileroglou@constellium.com (C. Tzileroglou), carla.barbatti@constellium.com (C. Barbatti), Hamid.Assadi@brunel.ac.uk (H. Assadi).

https://doi.org/10.1016/j.matchar.2025.114859
Received 18 October 2024; Received in revised form 7 February 2025; Accepted 17 February 2025
Available online 20 February 2025
1044-5803/

processing due to its ability to model complex, nonlinear relationships between process parameters, microstructure and mechanical properties [15]. Hsiang et al. [16] developed an artificial neural network (ANN) model to predict the tensile strength of extruded magnesium rectangular profiles based on selected processing parameters. Recently, Oien and Ringen [17] used a data-driven approach to predict the mechanical properties of extruded aluminium based on alloy composition and artificial ageing data. Extensive research has applied ML to predict material properties using alloy composition and basic processing parameters as features. However, there is a growing recognition that incorporating physical information, such as microstructure, is crucial for accurately capturing process-structure correlations [18]. While grain sizes can be readily used as an ML input feature, grain orientations (texture) require digitization into workable data, necessitating a new approach for texture analysis.

This study investigates the texture of six extrusion profiles produced on an industrial-scale extrusion line, using a combination of EBSD and XRD. The selected profiles include bulky shapes, such as round bar and townut, and thin profiles, such as flat bar and hollow rectangle, realistically representing extrusion profiles commonly used in industry. Compared to lab-scale extrusion, the friction between the billet and the tooling is substantially higher at the industrial-scale extrusion which operates at higher temperature and pressure. For instance, studies have shown that as billet temperature rises from 300 to 430 °C, the friction condition between billet and container interface can change from sliding to almost perfect sticking [19]. Research has also demonstrated that the friction factor increases with higher initial billet temperatures, varying from 0.65 at 300 °C to 0.91 at 450 °C after reaching peak pressure [20]. Consequently, higher shear deformation is experienced at the surface of the extrusion profile leading to a texture gradient in the cross-section.

This study examines the texture gradient from the centre to the edge of the extruded samples and provides a quantitative analysis of the cross-sectional deformation heterogeneity using three-dimensional FE analysis in DEFORM [21]. The experimental EBSD &XRD texture data were analysed using a novel method that categorizes textures into five distinct groups. By correlating the distribution of these groups to the FE deformation results, the study explores the impact of deformation modes on texture formation. The categorized texture data were subsequently used as input features in an ANN model to predict deformation modes in complex extrusion profiles, demonstrating the effectiveness of the proposed texture analysis method in digitizing EBSD and XRD data for ML applications.

2. Methods

2.1. Materials and investigated profiles

The billet material is an Al-Mg-Si-Cu alloy used in the automotive industry. The billets were produced by Direct Chill (DC) casting and homogenized at the Advanced Metal Casting Centre (AMCC) in Brunel University London. The initial texture of the billet is random. The size of the billet is 152 mm diameter and 420 mm long. Six extrusion profiles were investigated in this study: round bar, flat bar, hollow rectangle and solid thick shape (townut). For the round bar profile, three different diameters were investigated. Fig. 1 shows the geometry of the profiles.

2.2. Extrusion experiments

All extrusions were also performed at the AMCC. The DC cast billets were firstly heated to above 500° C then extruded on a horizontal extrusion press of 16 MN maximum press capacity. The container was held at 420 °C during the whole procedure. As a final step after extrusion, the material was immediately quenched using agitated water wave combined with sprays. Table 1 summaries the extrusion parameters used for each investigated profile.

2.3. Finite element simulation of extrusion

Aluminium extrusion is a thermo-mechanical process. The thermos-mechanical behaviour of the material flow during the hot extrusion was simulated using the commercial finite element software DEFORM. The extrusion processing is broadly characterised by three distinct stages: an initial transient state, during which the compressed billet material fills the die cavity and breaks through the die orifice, and a subsequent steady state that persists for the remainder of the process cycle. There is also an end transient state which occurs when about 80–90 % of the billet is extruded, leading to a rapid flow of billet material towards the die orifice. To ensure the quality of the extruded profile, a pre-determined length of the initial and final sections of the extrudate is

Table 1
Extrusion parameters for the investigated extrusion profiles.

Profile	Extrusion exit speed (m/min)	Exit T (°C)
Small round bar	9.3	548
Flat bar	9.6	545
Medium round bar	8.5	559
Big round bar	5.8	553
Tow nut	7.0	552

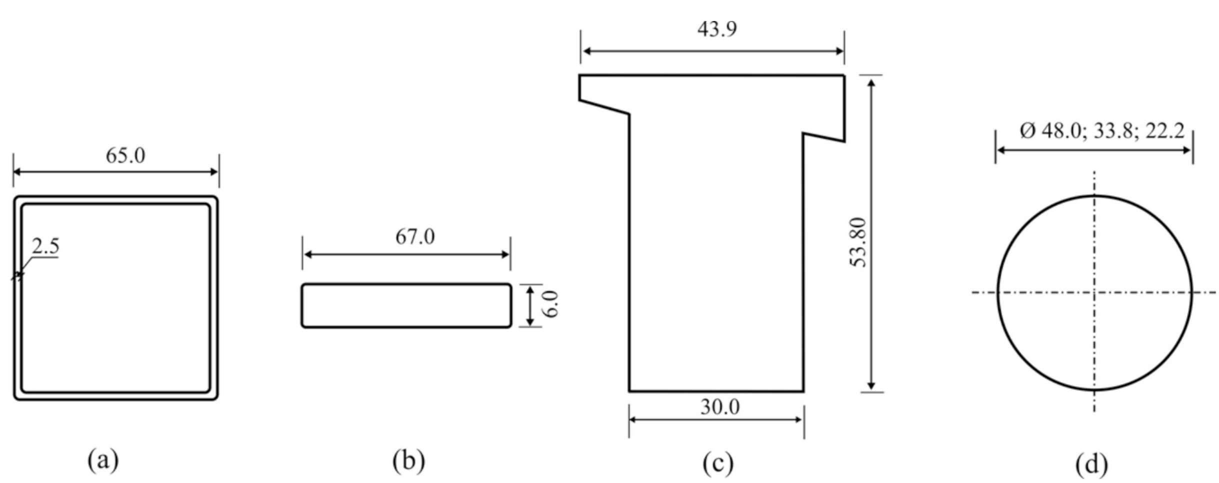

Fig. 1. Extrusion profiles investigated a) hollow rectangle, b)flat bar, c) townut, d) Round bars: small, medium and big (dimension in mm).

routinely removed on the processing line. Texture investigation is typically performed on samples obtained during the steady-state period of the extrusion process, when the material is subjected to a constant deformation rate and temperature. Therefore, an Arbitrary Lagrangian Eulerian (ALE) formulation model was considered appropriate to simulate the extrusion process of the flat bar and the medium round bar profile. Fig. 2 presents the three-dimensional FE model of the round bar profile. Taking advantage of structural symmetry, a quarter of the billet, ram and container were simulated. The symmetry plane boundary conditions were applied. Four-node tetrahedral element was used. Fine mesh of 0.5 mm was applied in the die region. Table 2 summarises the modelling parameters in the DEFORM simulation. A heat transfer coefficient of 10 kW/m^{2}K was assumed between the aluminium and the container and between the aluminium and the die face. The material property of aluminium 6082 from the DEFORM library was used in the study. The FE models were validated by comparing the simulation results of the extrusion pressure, velocity and exit temperature with the experimental data, where a good agreement was observed, as shown in Table 3.

2.4. Material characterization

The middle section of the extruded product, i.e., the extruded material of steady-state extrusion was investigated. To represent the texture of the extruded material, in this paper, the specimen frame of reference is defined with regard to the sample by its normal direction (ND), the extrusion direction (ED - analogous to the rolling direction RD), and the transverse direction (TD).

2.4.1. Electron backscatter diffraction (EBSD)

The microstructure and texture of the extruded material was studied with EBSD. Samples were taken from the extrusion-normal plane as illustrated in Fig. 3. The preparation for EBSD analysis included standard metallurgical grinding steps, and then polished to a 0.04 μm finish using an OPUS non-crystallising colloidal silica suspension (Metprep Ltd.), followed by electropolishing as a final step. For the electropolishing, a mixture of 30–70 % nitric acid-methanol was used, and the samples were immersed in it for 1 min at 12 V. EBSD analysis was performed on a Crossbeam 350 FIB-SEM (Carl Zeiss AG) equipped with a Hikari Plus EBSD camera (EDAX Inc.). The samples were tilted by 70^0 from horizontal axis and a 20 kV accelerating voltage was used. The scan step size was set to 0.5 μm. The scanned EBSD data were analysed with TSL-OIM Analysis software (EDAX Inc.).

2.4.2. X-ray diffraction pattern (XRD)

In selected cases, EBSD samples were further analysed for texture using XRD at the Constellium Technology Centre, at Vorppe France. XRD measurements were conducted in the normal-transverse plane. A Panalytical X'Pert Pro goniometer equipped with a copper ceramic X-ray tube and flat graphite monochromator was used. The goniometer is equipped with a collimator with parallel slit at 0.27^0 and polycapillary lens, φ 14 mm, calibrated with crossed slits. A voltage of 45 KV and a current of 40 mA was used.

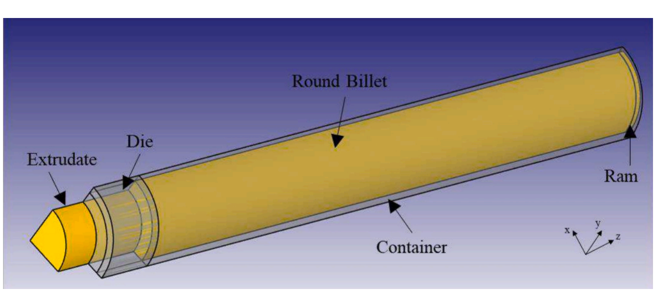

Fig. 2. Schematic view of the 3D finite element model of the round bar in DEFORM.

Table 2
Finite element model parameters.

Process parameters	Round die	Flat die
Billet length (mm)	250	250
Billet initial temperature (°C)	520	500
Die initial temperature (°C)	520	500
Ram initial temperature (°C)	520	500
Container initial temperature (°C)	450	420
Ram speed (mm/s)	6.4	2.9
Friction condition at container/ billet interface	No separation, shear 1.0	No separation, shear 1.0
Friction coefficient at die/billet interface	Separation, shear 0.4	Separation, shear 0.3

Sample preparation varied by profiles. For the flat bar, a sandwich structure was used while for the bulk profiles, a slice of the sample was sufficient. For the round bar, cross-section sliced in both the longitudinal and transverse directions were measured, while a single cross-section sliced in the transverse direction was used for the townut profile. The scanned XRD data were analysed using ATEX [22] analysis tool.

2.5. FE analysis results

Fig. 4 shows the distribution of plastic strain, include three normal and three shear components, in the cross-section at 15 mm after the die exit. The global Z axis of the FE model aligns with extrusion direction. The plastic strain components of material points along the Y axis in the cross-section of the medium round bar (Ø = 34 mm) are plotted in Fig. 4a. The X and Y axes represent two radial, axisymmetric directions. At the centre, ϵ_x and ϵ_y have the same negative values due to the symmetry of the round profile, indicating equal radial compression; the axial strain along extrusion direction, ϵ_z, is at its peak value and positive. The shear strain components are lowest at the centre, with ϵ_{xy} in the cross-sectional XY plane at zero, and the two out-of-plane shear components ϵ_{xz} and ϵ_{yz} having similar magnitudes but opposite signs.

Moving from the centre to the edge, ϵ_z gradually decreases to zero and becomes slightly negative at the edge, while ϵ_y gradually increases as a result of volume conservation. The in-plane shear strain ϵ_{xy} remains zero throughout while the ϵ_{yz} increases to its maximum value at the edge. Both ϵ_x and ϵ_{xz} remain constant for the material points along the Y axis. These results indicate that the material at the centre advances fastest and gradually slows approaching the periphery due to the friction at the die interface. The material of the medium round bar experiences the deformation mode equivalent to uniaxial axial tension at the centre, transitioning to shear deformation at the edge.

The plastic strain components across the thickness (along X axis) of the flat profile are plotted Fig. 4b. The most prominent feature in he strain distribution is its the uniformity across the thickness, with all plastic strain components showing minor increase from centre to surface, markedly different from the behaviour observed in the round profile. The compressive strain along the thickness (ϵ_x) is greater than that along the width (ϵ_y). The positive value of axial strain ϵ_z suggests that material at the centre of the die flows fastest, producing an axial tensile strain. The shear strain ϵ_{xy} and ϵ_{yz} remain nearly zero across the thickness, while ϵ_{xz} is the largest among all strain components. The axial strain results deviate from ideal plane strain compression due to the high tensile strain in the extrusion direction. Additionally, unlike in rolling where shear strain is zero at centre and peaks at the surface, the extruded flat profile exhibits significant shear strain at the centre, exceeding axial strain levels.

2.6. Microstructural analysis

2.6.1. Through thickness texture studied by EBSD

Fig. 5 presents IPF maps of the hollow rectangle scanned from the

Table 3
Experimental data vs. simulation results.

Die profile	Extrusion pressure (MPa), steady state		Exit velocity (mm/s), steady state		Exit temperature (°C), steady state	
	Measured	Simulated	Measured	Simulated	Measured	Simulated
Round	244	238	133	138	559	560
Flat	315	308	143	134	545	554

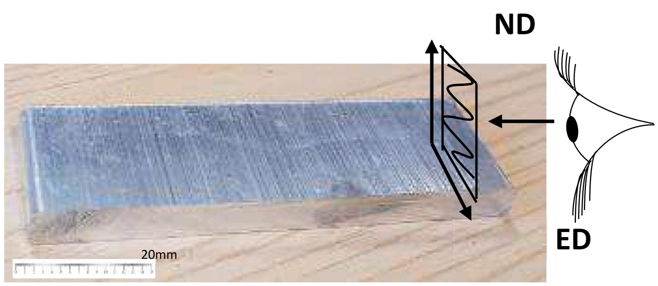

Fig. 3. Schematic representation of the plane used for EBSD scans of all the profiles.

inner to outer side, the flat bar scanned from top to bottom, and the medium round bar scanned from the centre to edge. To better characterise the texture through the thickness of the profile, the sample was extracted from the centre of the ND-TD cross-section, as illustrated in Fig. 5, to minimise the edge effects. Fig. 6 depicts multiple scans of the townut, divided into three areas as shown in Fig. 6a, with approximately 33 mm out of the total 54 mm profile length scanned. EBSD was conducted on the middle area of the townut's cross-section, covering a smaller region than that investigated by XRD. These EBSD maps were obtained from the ND-ED plane, and the IPF plots were plotted to show the ED with respect to the crystallographic axes.

The colour coding in the IPF maps suggest a similar texture distribution between the hollow rectangle and the flat bar. In contrast, the round bar exhibits a non-uniform texture distribution in its cross-

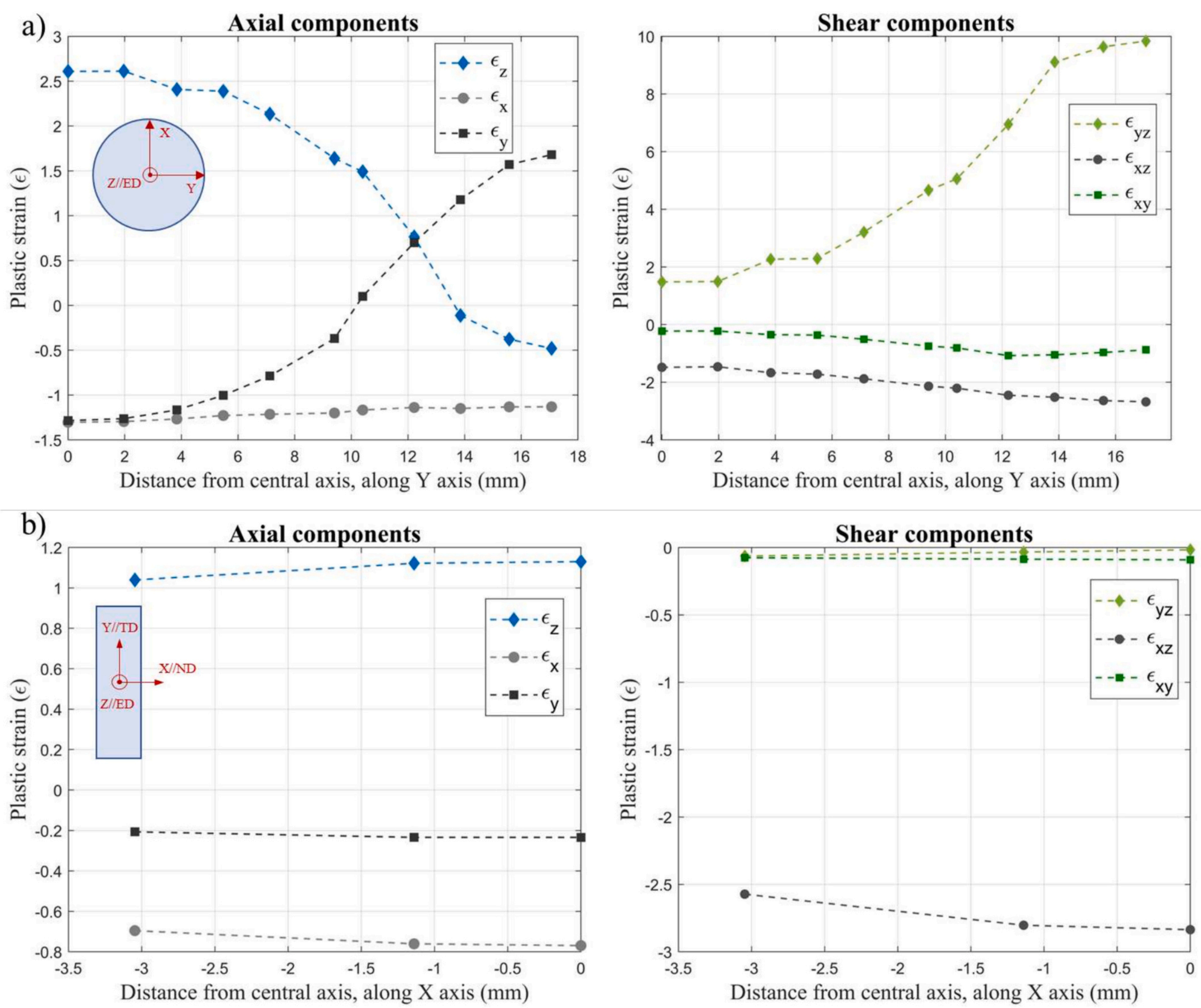

Fig. 4. Effective strain results of FE models a) medium round bar, b) flat bar.

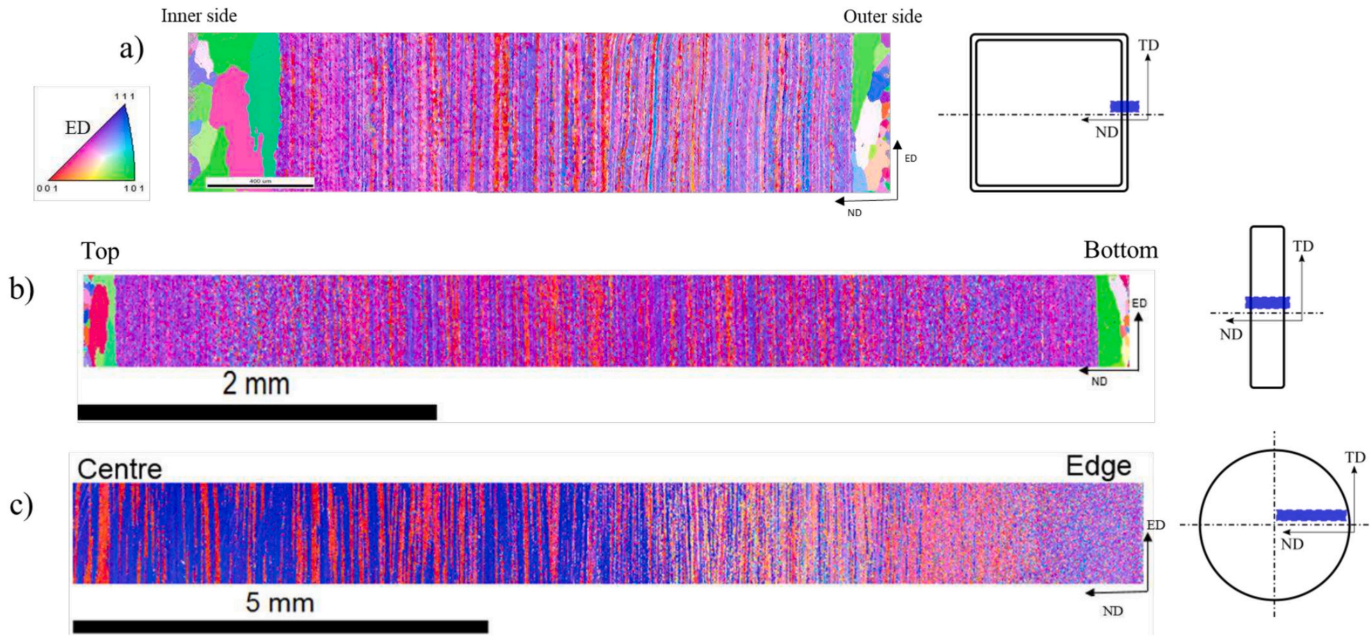

Fig. 5. IPF maps of the whole cross section of a) hollow rectangle and b) flat bar c) half cross section of the medium round bar.

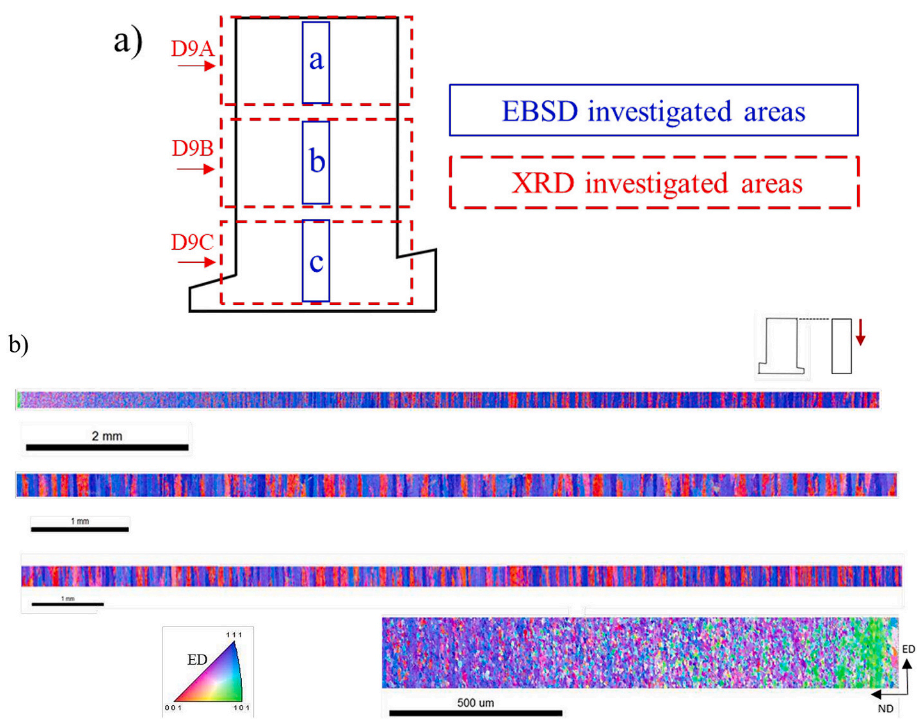

Fig. 6. Townut profile: a) segmented into three area for EBSD and XRD measurements b) EBSD IPF maps of areas a, b, c and edge of c.

section. The texture distribution of the townut also exhibits non-uniformity, with the top edge of area a and the very edge of area c displaying similar crystallographic textures, distinct from other regions.

3. Discussion

3.1. Texture analysis using a novel method

3.1.1. A novel texture analysis method

Texture component analysis method is widely used for FCC alloys to study grain orientation changes as a function of thermomechanical treatment. The traditional texture component analysis reduces the representation of the orientation distribution into a small set of ideal orientations, commonly observed in rolling process. An ideal orientation ({hkl} < uvw>),such as Brass({110} ⟨112⟩), means that the crystallographic {hkl}plane is parallel to the rolling plane (ND) and the crystallographic <uvw> direction is parallel to the rolling direction.

The traditional approach presented challenges in this study. First, inconsistencies were observed in the percentage of grain orientations identified across EBSD and XRD scans, particularly among different extrusion profiles, which madebit difficult to achieve consistent 100 % orientation identification. Secondly, the number of texture components required for accurate identification varied; for instance, while Brass and Cube components might account for 70 % of grain orientations in one scan, an additional S component was needed to reach a similar level in another. These inconsistencies post a major obstacle for comparative analysis, as reliably detecting differences is crucial before assessing the underlying causes.

To address this issue, this paper proposes a novel texture analysis method. A list of orientations was constructed based on Miller indices, as summarised in Table 4. The list categorizes orientations into five groups. Focusing on crystallographic direction in the extrusion direction, Group 1 encompasses orientations with <100>//ED, Group 2 with ⟨1−10⟩//ED, Group 3 with ⟨−1−11⟩//ED, Group 4 with ⟨2−11⟩//ED and Group 5 represents higher order crystallographic directions. This grouping naturally reveals classic rolling texture components: Cube and Goss appear in Group 1, Copper in Group 3, and Brass and S in Group 4. It is noted that it is the (123)[6 3–4] orientation often quoted as the characteristic S component [23], however there is only 8 degrees difference between the characteristic S orientation and the orientation of (−1 2 4)[2−11].

The proposed list was implemented in the OIM software to calculate the volume fraction of specified orientation with a tolerance of 15°, based on the Crystal Orientation Map. For Group 1 texture components, a tolerance of 30° was applied to improve the identification of subgrain orientations. A total number of 64 EBSD scans of 6 extrusion profiles were analysed. Table 5 summarises the average percentage of orientations identified for each profile, demonstrating that identification rates consistently exceeded 98 % across all scans. For XRD scans, the proposed method was implemented in the ATEX software to calculate the volume fractions based on the discretised orientation list. As shown in Table 6, consistent grain orientation identification was achieved. This novel texture analysis method provides a comprehensive and structured representation of crystallographic orientations in a simplified format, making it well-suited suited for machine learning applications.

3.1.2. Analysis results of EBSD

The EBSD scan of the half cross-section of the medium round bar was segmented into 13 strips to analyse texture variation using the Crystal Orientation Map in OIM, which have been included in Appendix A. The analysis focused on the texture distribution of the five groups. Fig. 7 compares the volume fraction of each group at the centre and the edge of the medium round bar. Two distinctive distribution patterns were observed: group 3 is the dominant feature at the bar centre followed by Group 1, while Group 4 is predominant at the edge of the profile. Group 2 and 5 are absent at the bar centre and show minimal presence at the edge (0.02 for Group 2 and 0.03 for Group 5).

Table 4
List with proposed grain orientation identification.

Group	Group	(hkl)[uvw]	Euler angles	Texture component
1	⟨100⟩	(001)[100]	(0.0, 0.0, 0.0)	Cube
		(011)[1 0 0]	(0.0, 45.0, 0.0)	Goss
		(021)[1 0 0]	(0.0, 63.4, 0.0)	
2	⟨1−11⟩	(0 0 1)[1−10]	(45.0, 0.0, 0.0)	
		(111)[1−1 0]	(0.0, 54.7, 45.0)	
3	<−1−1 1>	(101)[−1−11]	(54.7, 45.0, 90.0)	
		(112)[−1−1 1]	(90.0, 35.3, 45.0)	Copper
		(1 2 3)[−1−1 1]	(105.0, 36.7, 26.6)	
4	<2−1 1>	(0 1 1)[2−1 1]	(35.3, 45.0, 0.0)	Brass
		(10−2)[2−1 1]	(65.9, 153.4, 90.0)	
		(23−1)[2−1 1]	(25.1, 105.5, 33.7)	
		(−1 2 4)[2−1 1]	(56.8, 29.2, 333.4)	S
5	Higher order	(2 1−4)[3−21]	(33.2, 150.8, 63.4)	
		(231)[5−4 2]	(18.0, 74.5, 33.7)	

Table 5
Grain orientations identified in the EBSD scan using the proposed method.

Profile	No. EBSD scans	Avg % orientations identified
Small bar	14	98.00 %
Medium bar	13	97.80 %
Big bar	20	97.80 %
Flat bar	12	99.30 %
Townut	3	96.00 %
Hollow	2	99.30 %

Table 6
Grain orientations identified in the XRD scan using the proposed method.

Profile	No. EBSD scans	Avg % orientations identified
Small bar	14	98.00 %
Medium bar	13	97.80 %
Big bar	20	97.80 %
Flat bar	12	99.30 %
Townut	3	88.00 %
Hollow	2	99.30 %

Figure *8*Figure 8a and b compare the distribution of volume fractions of Groups 1, 3 and 4 in the cross section of the flat and medium round bar. The EBSD scan of the flat bar was divided into small strips and analysed in OIM using Crystal Orientation map as included in Appendix A. Groups 2 & 5 were not included in this comparison due to negligible volume fractions observed. The combined volume fraction of Group 1 and 3 is also analysed for reference. In the flat bar, the group distributions remain nearly uniform across the thickness with Group 4 as the dominant feature, exhibiting an average volume fraction above 0.6. The sum of Groups 1 and 3 is highest at the centre and decreases slightly towards the edge. In the medium round bar, it is interestingly observed that the sum of the volume fraction of Group 1 and 3 is close to 1.0 at the centre; and the two groups exhibiting an inverse relationship until both start to decline towards the edge. This phenomenon is analogous to the deformation texture commonly observed in copper wire drawing, where ⟨111⟩ and ⟨100⟩ fibre are found to be parallel to the drawing direction [24]. Group 4 is nearly absent at the centre of the round bar, while increased to more than 0.6 at the edge.

Fig. 8b, c and d present a comparative analysis of the spatial distribution of volume fractions for Groups 1, 3 and 4 in the cross-sections of small, medium and big round bars. All samples display similar patterns; however, in the small bar, the sum of Groups 1 and 3 decreases at an earlier stage, whereas the big bar exhibits an extended region in which this sum remains close to unity. Furthermore, the inverse relationship between Group 1 and 3 is most prominent in the region where their sum approaches unity.

There has been a long-standing conversation in the literature regarding the source of cube texture component in deformed high-stacking fault energy metals (Al and Cu), particularly regarding its relationship with Copper and S textures [25–30]. The analysis in Fig. 8 suggests that Group 3 can transform into Group 1 during axial tensile deformation, supporting the literature that Copper texture leads to Cube formation.

3.1.3. Analysis results of XRD

The volume fraction of the five groups obtained from XRD scans is compared with that from EBSD scans in Fig. 9. Similar distributions for thin profiles, such as the flat bar and hollow rectangle, as shown in Fig. 9a and b. For the round bar (Fig. 9c), the XRD scan in the longitudinal direction closely matches the EBSD results at the centre, while the XRD transverse direction aligns with the EBSD edge results. In the townut profile (Fig. 9d), XRD measurements show comparable volume

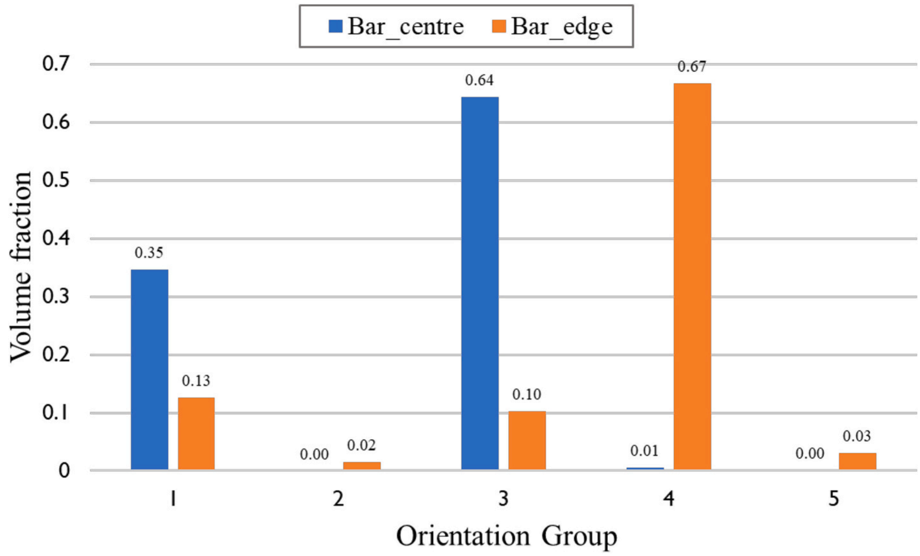

Fig. 7. Volume fraction of each orientation group at the centre and edge of the medium round bar.

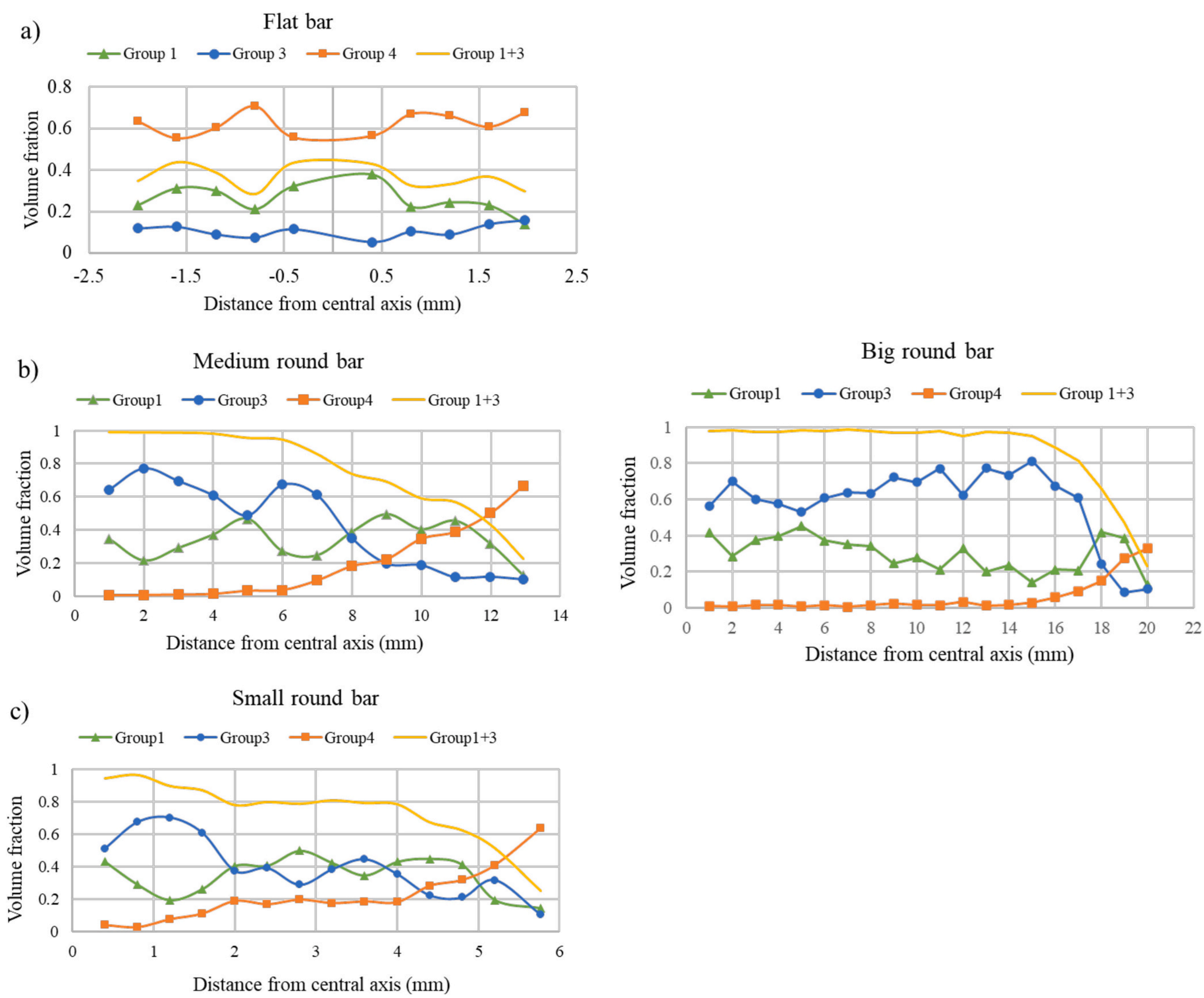

Fig. 8. Spatial distribution of volume fractions of Group 1, 3 & 4 in the cross section of a) flat bar b) medium round bar, c) small round bar, d) big round bar.

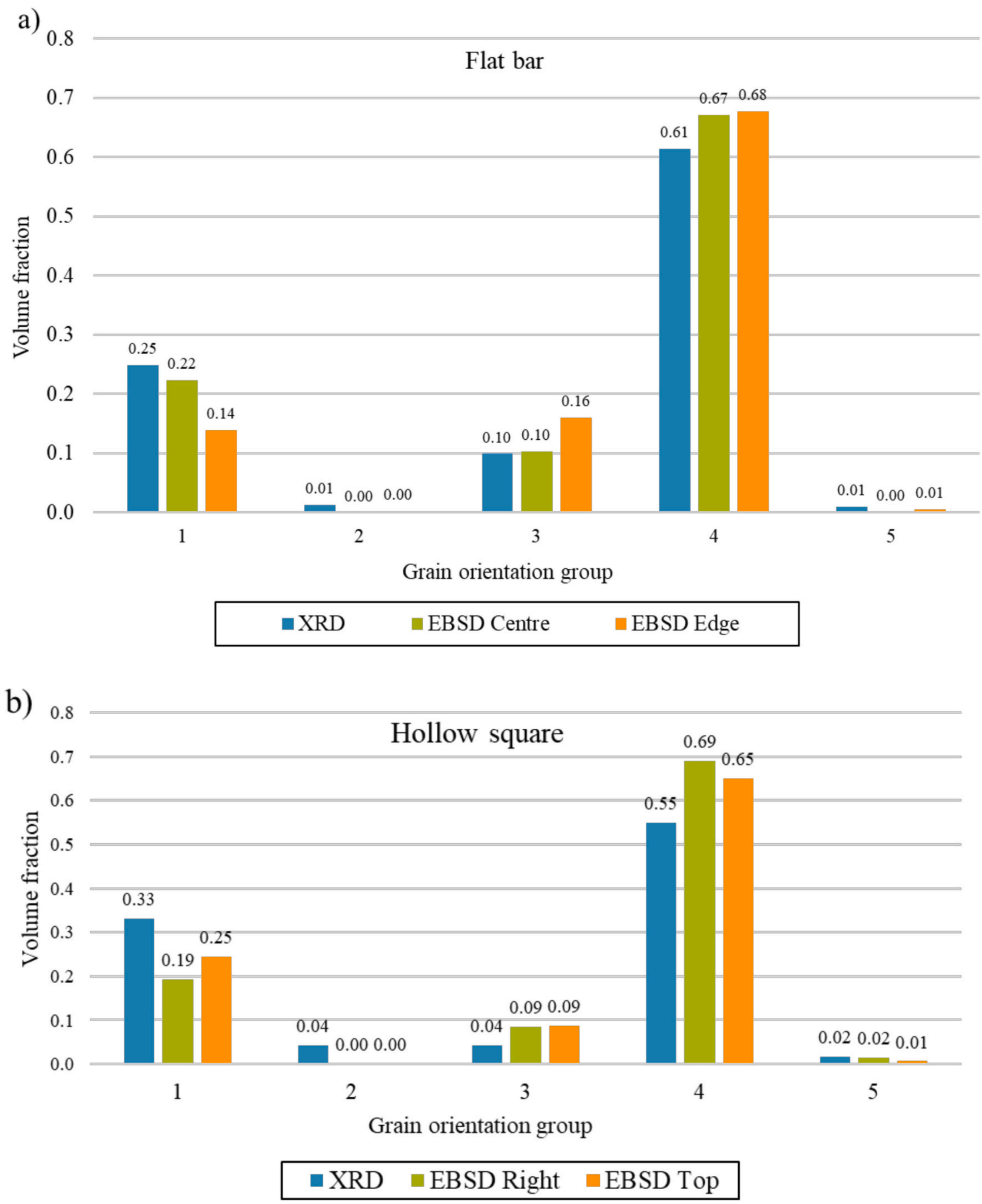

Fig. 9. Distribution of volume fractions of five groups from XRD scan compared to EBSD scans a) flat bar b) Hollow rectangle and c) Medium round bar d) Townut.

fractions across regions A, B, C, with high fractions of Group 1 and 3. Compared to XRD, EBSD results exhibit a higher volume fraction of Group 3 and lower Group 4. Both XRD and EBSD results show that the central region has a lower fraction of Group 1 and a higher fraction of Group 4 texture components. The observed discrepancy is attributed to differences in the measurement areas used for EBSD and XRD, as illustrated in Fig. 6a.

Overall, for thin profiles EBSD and XRD measurements provide comparable results, however, for bulky profiles, noticeable discrepancies are observed, as XRD captures bulk texture. Nevertheless, texture analysis of XRD scans also reveals two distinct texture distribution patterns: thin profiles are predominantly characterised by Group 4, whereas bulky profiles exhibit a high volume fraction of Group 3. This comparative analysis demonstrates that the novel texture analysis method is applicable to both EBSD and XRD scan data and can significantly improve the reliability of comparative analyses.

3.2. Effect of deformation modes on texture

The FE results in Fig. 4 reveal the complexity of extrusion deformation, highlighting cross-sectional inhomogeneity and its dependence on profile shape. By correlating the plastic strain with the texture variation in the cross-section analysed using EBSD, valuable insights are gained into how deformation modes influence texture development.

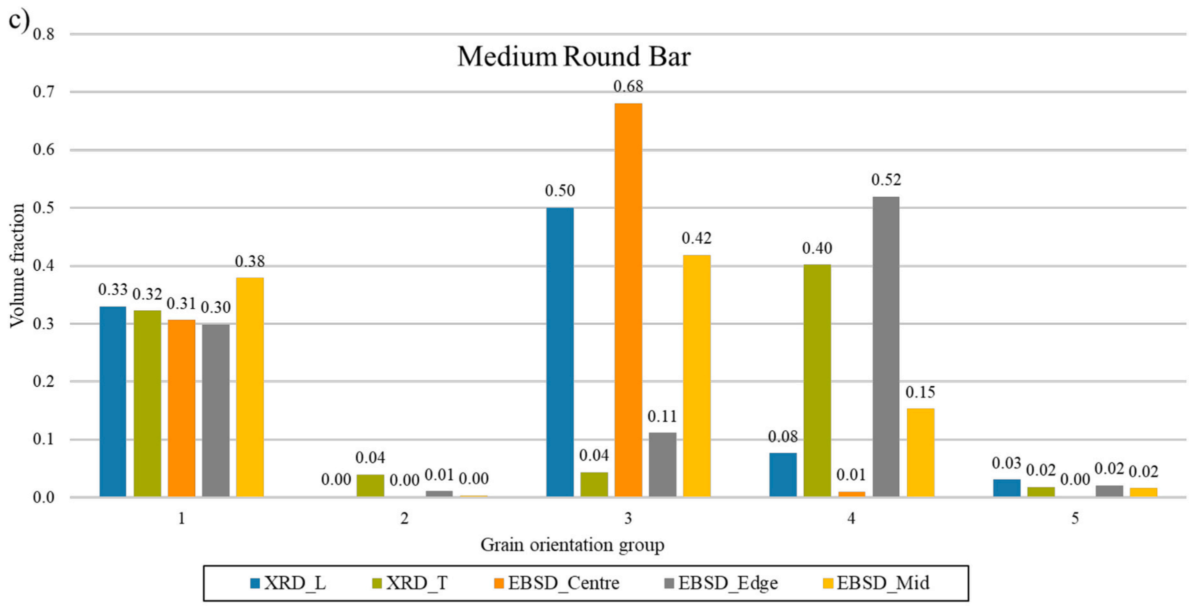

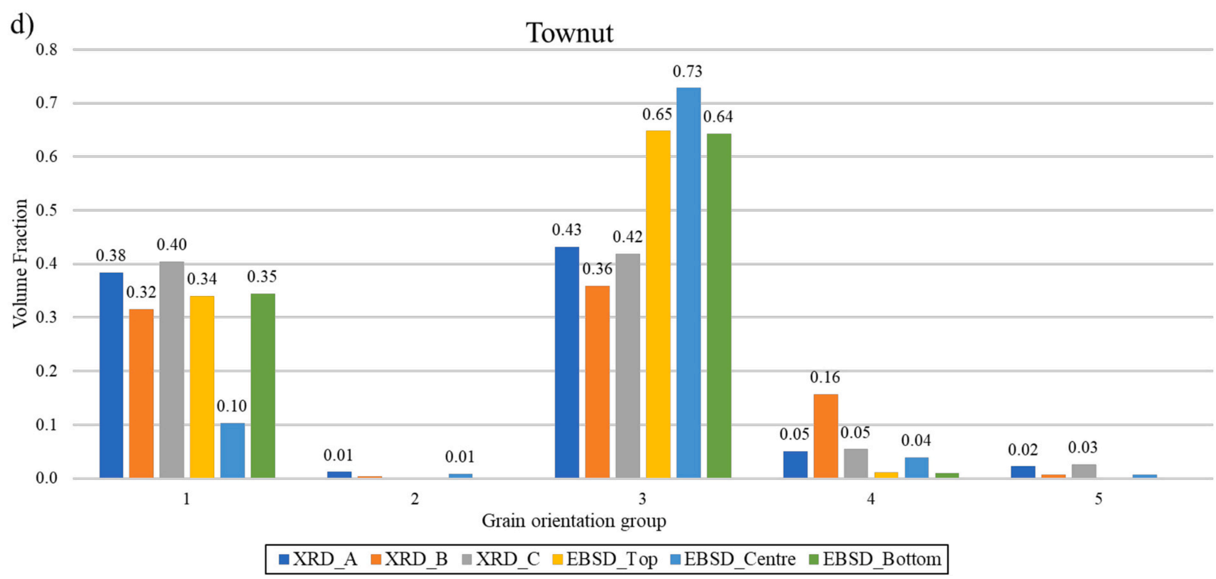

Fig. 9. (*continued*).

The normal strain results at the centre of the round bar centre suggest a uniaxial tensile deformation mode that is analogous to axisymmetric tensile deformation. The observed combination of Group 1 (<100>//ED) and Group 3 (<111>//ED) texture components at the bar centre aligns with the <111> and < 100> fibre components reported for ideal axisymmetric tension deformation obtained through viscoplastic self-consistent modelling [31]. Towards the bar edge, the deformation mode shifts to shear dominance, with shear strain exceeding axial strains by more than four times. Correspondingly as shown in Fig. 7, the volume fraction of Group 3 drops substantially from 0.64 at the centre to 0.1 at the edge, while Group 1 decreases from 0.35 to 0.13. The most significant development is the appearance of Group 4 textures (<211>//ED), from 0.01 at the centre to 0.67 at the edge. Thus, shear deformation at the bar edge produces a strong <211>//ED with weak <100> and < 111>//ED components. The gradual transition from uniaxial tensile to shear deformation-dominant leads to a corresponding variation in texture distribution. In regions of the round bar centre where uniaxial tension prevails, <100> and < 111> //ED components account for nearly 100 % of the crystal orientations, with <111> being more prominent, as seen in Fig. 8b, c and d. In the transitional regions, as tensile deformation wanes, the combined volume fraction of <100> and < 111> decreases, yet the <100>//ED component becomes relatively stronger.

The deformation mode of the flat bar displays minimal variation across the thickness and resembles that of the edge of round bars: characterised by high shear deformation with minor axial deformation. This complex deformation mode is unique to extrusion and different from rolling. The texture distribution in the flat bar is dominated by Group 4, with a volume fraction exceeding 0.6, while Groups 1 and 3 together constitute the remaining fraction. Further analysis reveals that Group 4 primarily is contributed from Brass and S components. In other words, the flat bar exhibits strong Brass and S texture components combined with weak <100> and < 111>//ED components. This texture distribution differs from typical rolling textures, as it lacks the significant Copper component characteristic of copper-type rolling textures and the Goss component commonly found in brass-type rolling textures.

The FE plastic strain results for the flat bar and the edge of the round bar, along with their similar texture distributions, indicate a strong correlation between shear strain and < 211>//ED texture components, while the duplex <100> and < 111> fibre textures are associated with axial tensile strain. Although in-plane axial strains are compressive, they are relatively low compared to the shear strain at the same location. This explains the absence of ⟨110⟩ fibre texture components, which are typically observed for uniaxial compression and plane strain compression [23] but not in the extruded profiles.

The analysis of FE results and texture distribution reveals that friction plays a key role in forming extruded texture. Friction between billet and tooling significantly slows the material flow in the peripheral regions, subsequently resulting in tension in the extrusion direction at the centre. At the high temperature of extrusion, friction-induced shear deformation can dominate the entire cross-section of thin profiles, while bulky profiles exhibit a transition from shear deformation at the edge to uniaxial tension at the centre. Shear deformation induces <211>//ED texture components whereas uniaxial tension produces a combination of <111> and < 100>//ED texture components. In the tension dominated region, the combined volume fraction of <111> and < 100> groups remain 1.0, though each group fluctuates inversely.

As seen in Fig. 8c, Group 4 texture components (<211>//ED) begin to increase steadily within 1 mm from the centre of the small round bar, indicating a shear-dominated deformation region extending over 5 mm from the edge. Similarly, shear-dominated regions of approximately 6 mm are observed for the medium and big round bars (Fig. 8b and d). These findings suggest an upper boundary for the friction-induced shear deformation zone, further explaining the predominance of shear deformation in thin profiles, such as the 6 mm thick flat bar and 2.5 mm thick hollow rectangle.

3.3. Application of novel texture data in an ANN model for deformation mode prediction

The digitised texture data obtained using the new texture analysis method was applied in the development of an artificial neural network (ANN) model. Constructed in the TensorFlow [32] framework within Python, the ANN model aims to predict deformation modes in complex profiles used in the automobile industry, bypassing the need for time-consuming finite element analysis. The ANN model classifies the investigated region as either axial tensile-dominant or shear-dominant, offering insights into the deformation mechanisms during extrusion and contributing to a comprehensive understanding of the extrusion conditions. This approach paves the way for automated material optimization on the processing line.

3.3.1. Training data acquisition

Texture data, calibrated using the method outline in Section 3.1 were acquired for model training. The input of each data point comprises the texture distribution of the five proposed groups derived from EBSD or XRD scans as shown in Appendix A. The two output classes, axial tensile and shear, are labelled as 1 and 0, respectively, based on the cross-sectional strain output of the finite element analysis. Specifically, the central regions of round bars are classified as axial tensile while the thin flat profiles (flat bar &hollow rectangle) and the edge regions of round bars are classified as shear-dominant. A total of 51 labelled data points were collected for training. The labelled data points were partitioned into a training set (70 %) and a cross-validation set (30 %). Additionally, 22 unlabelled data points, collected from the transitional regions of the round bars and the townut profile, were used as the test set.

3.3.2. Designing the ANN

Detailed information about artificial neural networks, how they are built, trained, and used are available in the literature [33,34]. In brief, ANNs are composed of interconnected artificial neurons. Each neuron receives numerical inputs, either raw data or outputs from other neurons, applies associated weights and biases to the input and subsequently processes them through a mathematical function. The resulting outputs are then transimitted along to other neurons. During training, these weights and biases are adjusted to improve the predictive accuracy of the ANN.

There are many types of ANN, we selected the multilayer perceptron ANN with two hidden layers, trained with the backpropagation algorithm, based on several experimental trials. Machine learning algorithms have two types of variables that affect the performance of the model, parameters and hyperparameters. Parameters are model variables whose values can change during the training, such as weights and biases. On the other hand, hyperparameters, including the number of neurons in each hidden layer, are set prior to training. We used grid search to determine the optimal combination of the number of neurons in the first and second layers. Different combinations were evaluated based on their classification error which is defined as the number of misclassified examples over the total number of examples. The optimal ANN architecture is comprised of 10 neurons in the first hidden layer and 2 neurons in the second hidden layer. A misclassification error of less than 0.1 % was achieved for both the training and cross-validation sets. Other hyperparameters of the ANN were set following the conventional practice. The input features consist of the texture distribution of the five proposed groups, which were not normalised because the volume fraction inherently lies within the range of [01]. The rectified linear unit (ReLu) activation function was adopted. We used the Sparse Categorial Crossentropy loss function combined with the softmax function to compute the probability of the classification. Adaptive moment estimation (Adam) optimisation algorithm [35] was used.

3.3.3. Predictions and discussions

The ANN model was first adopted to predict the deformation mode in the transitional region between the centre and edge of the three round bars, where the mode is unclear. Fig. 10 shows the predicted probability of axial tension across this region, with the large bar displaying the widest axial tension zone, while the small bar shows the narrowest zone and exhibits several fluctuations rather than a smooth transition. These results suggest that material flow is fastest at the centre of round bar profiles, with more uniform cross-sectional flow velocity in the large bar. Friction at the billet-die interface causes the deformation mode to shift from axial tension at the centre to shear at the edge. As the bar diameter decreases, the shear region occupies a larger portion of the cross-section, leading to stronger internal shear forces and increased sliding between the centre and edge of the material flow as observed in the small round bar.

The ANN was also used to predict the deformation modes in the townut profile based on both EBSD and XRD scans. Table 7 summarises the predicted probabilities of axial tension/shear for the investigated regions as illustrated in Fig. 6a. Differences in predictions were observed between the two data sources. The EBSD data suggest the investigated area under axial tension, whereas the XRD data indicate a mix of axial tension and shear in region A and B and primarily tension in region C. These discrepancies are attributed to the fact that XRD measured bulk texture of larger regions compared to the middle area examined by EBSD (Fig. 6a). Consequently, XRD captured Group 4 textures linked to shear deformation near the edge, highlighting the inhomogeneous plastic strain distribution across the cross-section. The predicted deformation modes in townut profile is similar to that in the round bar, further contributing to the understanding of extrusion deformation of bulky profiles.

4. Conclusions

This paper investigated the extruded texture of 6xxx aluminium alloys produced on an industrial scale press using a combination of physics-based modelling and machine learning supported by experimental investigation using EBSD and XRD. Finite element analysis of the

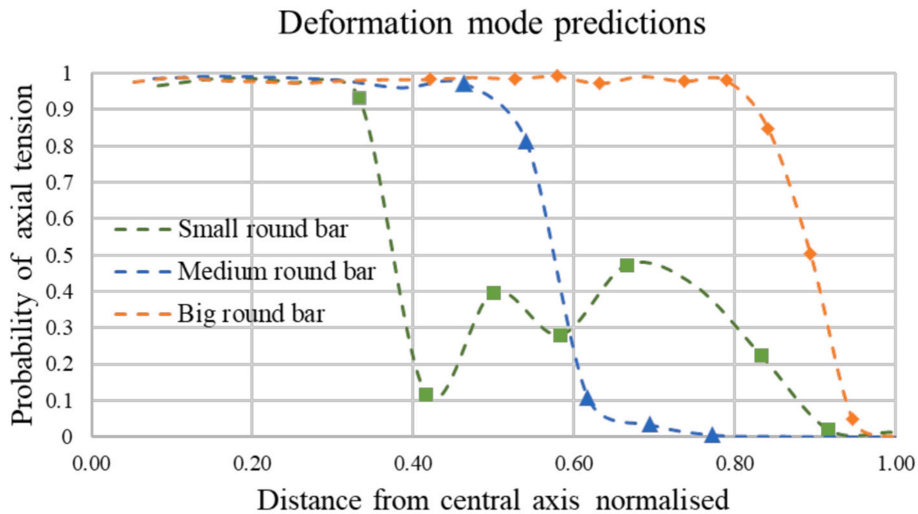

Fig. 10. Predicted deformation in the cross-section of round bars.

Table 7
ANN predictions of deformation mode in townut cross-section.

Data source	Region	Probability of axial tension	Probability of shear
	a	100.0 %	0.0 %
EBSD	b	95.6 %	4.4 %
	c	100.0 %	0.0 %
	D9A	40.2 %	59.8 %
XRD	D9B	40.8 %	59.2 %
	D9C	98.1 %	1.8 %

extrusion deformation of a typically thin (flat bar) and a typically bulky profile (medium sized round bar), revealed distinct deformation modes for the two types of profiles and inhomogeneous deformation in the cross-section.

A novel texture analysis method was developed in this study for identifying and categorising texture distributions in EBSD and XRD scans. The method was successfully implemented in OIM for EBSD and ATEX for XRD analysis, enabling consistent digitization of texture data and enhancing the training dataset for machine learning applications. The texture analysis discovered that the thin extruded profiles are dominated by <211>//ED texture components, and is different from typical rolling textures, as it lacks the significant Copper component characteristic of copper-type rolling textures and the Goss component commonly found in brass-type rolling textures. In round bars, the texture transitioned from a combination of <111> and < 100>//ED components at the centre to <211>//ED textures towards the edge. Additionally, it was observed that the duplex <111> and < 100> fibber components in the axial tension-dominated region exhibit an inverse transformation relationship.

Correlating the FE plastic strain results with the texture analysis revealed that in extrusion, the friction-induced shear deformation induces <211>//ED texture components whereas tensile deformation at the centre of profiles produces a combination of <111> and < 100>// ED texture components. The analysis of FE results and texture distribution highlighted friction as a key factor in extruded texture formation. High friction between billet and tooling at industrial scale induces large shear deformation zone that can prevail the entire cross-section of thin profiles, or result in a notable transition from shear at surface to uniaxial tension at the centre in the bulky profiles.

The texture distribution of the five proposed groups were adopted as input features in an ANN model developed to predict the deformation modes based on experimental texture data. The ANN model, successfully validated, was applied to predict the extrusion deformation of a complex townut profile, revealing that the material flow velocity is higher in the middle region and decreases towards edge, consistent with observations in other bulky profile shapes.

CRediT authorship contribution statement

Mian Zhou: Writing – original draft, Visualization, Validation, Software, Methodology, Investigation, Formal analysis, Data curation. **Chrysoula Tzileroglou:** Writing – review & editing, Project administration, Investigation, Data curation. **Carla Barbatti:** Writing – review & editing, Supervision, Resources, Project administration, Methodology, Funding acquisition, Conceptualization. **Hamid Assadi:** Writing – review & editing, Supervision, Resources, Project administration, Methodology, Funding acquisition, Conceptualization.

Declaration of competing interest

The authors declare the following financial interests/personal relationships which may be considered as potential competing interests:

Mian Zhou reports financial support was provided by Engineering and Physical Sciences Research Council. Mian Zhou reports financial support was provided by Constellium. If there are other authors, they declare that they have no known competing financial interests or personal relationships that could have appeared to influence the work reported in this paper.

Acknowledgement

Authors thankfully acknowledge financial support of the EPSRC Materials Made Smarter Centre (Reference EP/V061798/1).

Appendix A. Supplementary data

Supplementary data to this article can be found online at https://doi.org/10.1016/j.matchar.2025.114859.

Data availability

The data supporting this study are available upon request, subject to approval from the project's industrial sponsor, Constellium.

References

[1] B. Simhachalam, K. Srinivas, C.L. Rao, Energy absorption characteristics of aluminium alloy AA7XXX and AA6061 tubes subjected to static and dynamic axial

load, Int. J. Crashworthiness 19 (2) (2014) 139–152, https://doi.org/10.1080/13588265.2013.878974.
[2] P. Mukhopadhyay, Alloy designation, processing, and use of AA6XXX series Aluminium alloys, Int. Sch. Res. Not. 2012 (1) (2012) 165082, https://doi.org/10.5402/2012/165082.
[3] D. Paraskevas, K. Kellens, W. Dewulf, J.R. Duflou, Environmental modelling of aluminium recycling: a life cycle assessment tool for sustainable metal management, J. Clean. Prod. 105 (2015) 357–370, https://doi.org/10.1016/j.jclepro.2014.09.102.
[4] M. Zhou, et al., Chapter 9 - intelligent processing and development of high-performance automotive aluminum alloys: Application of physics-based and data-driven modeling, in: M.A. Zikry (Ed.), Innovative Lightweight and High-Strength Alloys, Elsevier, 2024, pp. 257–322, https://doi.org/10.1016/B978-0-323-99539-9.00009-6.
[5] L. Zhang, et al., Texture, microstructure and mechanical properties of 6111 aluminum alloy subject to rolling deformation, Mater. Res. 20 (5) (2017) 1360–1368, https://doi.org/10.1590/1980-5373-MR-2017-0549.
[6] M.K. Sumeet Mishra, A. Singh, Evolution of rotated Brass texture by cross rolling: implications on formability, Mater. Sci. Technol. 36 (12) (2020) 1272–1281, https://doi.org/10.1080/02670836.2020.1773036.
[7] W.H. Van Geertruyden, W.Z. Misiolek, P.T. Wang, Grain structure evolution in a 6061 aluminum alloy during hot torsion, Mater. Sci. Eng. A 419 (1) (2006) 105–114, https://doi.org/10.1016/j.msea.2005.12.018.
[8] A. Foydl, A. Segatori, A.E. Tekkaya, Grain size evolution simulation in aluminium alloys AA 6082 and AA 7020 during hot forward extrusion process, Mater. Sci. Technol. 29 (1) (2013) 100–110, https://doi.org/10.1179/1743284712Y.0000000132.
[9] S. Kaneko, K. Murakami, T. Sakai, Effect of the extrusion conditions on microstructure evolution of the extruded Al–Mg–Si–Cu alloy rods, Mater. Sci. Eng. A 500 (1) (2009) 8–15, https://doi.org/10.1016/j.msea.2008.09.057.
[10] K. Zhang, K. Marthinsen, B. Holmedal, T. Aukrust, A. Segatori, Through thickness variations of deformation texture in round profile extrusions of 6063-type aluminium alloy: experiments, FEM and crystal plasticity modelling, Mater. Sci. Eng. A 722 (2018) 20–29, https://doi.org/10.1016/j.msea.2018.02.081.
[11] Y. Sun, X. Bai, D. Klenosky, K. Trumble, D. Johnson, A study on peripheral grain structure evolution of an AA7050 aluminum alloy with a laboratory-scale extrusion setup, J. Mater. Eng. Perform. 28 (8) (2019, Aug) 5156–5164, https://doi.org/10.1007/s11665-019-04208-7.
[12] T. Furu, H.E. Vatne, Texture evolution during extrusion of flat AA6060 and AA6082 aluminium profiles, Mater. Sci. Forum 273–275 (1998) 403–410, https://doi.org/10.4028/www.scientific.net/msf.273-275.403.
[13] P. Saha, Aluminum Extrusion Technology, ASM International, 2000.
[14] L. Donati, B. Reggiani, R. Pelaccia, M. Negozio, S. Di Donato, Advancements in extrusion and drawing: a review of the contributes by the ESAFORM community, Int. J. Mater. Form. 15 (3) (2022, May), https://doi.org/10.1007/s12289-022-01664-w.
[15] A. Stoll, P. Benner, Machine learning for material characterization with an application for predicting mechanical properties, GAMM Mitteilungen 44 (1) (2021, Mar), https://doi.org/10.1002/gamm.202100003.
[16] S.H. Hsiang, J.L. Kuo, F.Y. Yang, Using artificial neural networks to investigate the influence of temperature on hot extrusion of AZ61 magnesium alloy, J. Intell. Manuf. 17 (2) (2006, Apr) 191–201, https://doi.org/10.1007/s10845-005-6636-0.
[17] C. Dalheim Øien, G. Ringen, Manufacturing Letters Data-driven through-process modelling of aluminum extrusion: predicting mechanical properties, 2024 [Online]. Available, www.sciencedirect.com.
[18] J. Peng, Y. Yamamoto, J.A. Hawk, E. Lara-Curzio, D. Shin, Coupling physics in machine learning to predict properties of high-temperatures alloys, NPJ Comput. Mater. 6 (1) (2020, Dec), https://doi.org/10.1038/s41524-020-00407-2.
[19] L. Wang, J. Zhou, J. Duszczyk, L. Katgerman, Friction in aluminium extrusion - part 1: a review of friction testing techniques for aluminium extrusion, Tribol. Int. 56 (2012) 89–98, https://doi.org/10.1016/j.triboint.2012.01.012.
[20] I. Flitta, T. Sheppard, Nature of friction in extrusion process and its effect on material flow, 2003, Jul, 01, https://doi.org/10.1179/026708303225004422.
[21] Scientific forming technologies corporation, in: Design Environment for FORMing, DEFORM v13.0.1, 2023.
[22] B. Beausir, J.-J. Fundenberger, Analysis Tools for Electron and X-Ray Diffraction, ATEX-Software. www.atex-software.eu, 4.12.
[23] Texture and Anisotropy Preferred Orientations in Polycrystals and their Effect on Materials Properties (U. F. Kocks) (z-lib.org), 2025.
[24] H. Park, D.N. Lee, The Evolution of Annealing Textures in 90 Pct Drawn Copper Wire, 2025.
[25] S. Chakraborty, C.S. Patil, S.R. Niezgoda, Development of the cube component ({001} ⟨ 100 ⟩) during plane strain compression of copper and its importance in recrystallization nucleation, Metall. Mater. Trans. A Phys. Metall. Mater. Sci. 53 (2) (2022) 503–522, https://doi.org/10.1007/s11661-021-06513-0.
[26] A. Akef, J.H. Driver, Orientation splitting of cube-oriented face-centred cubic crystals in plane strain compression, 2025.
[27] K. Kashihara, Y. Tsujimoto, D. Terada, N. Tsuji, Texture evolution in {112} <111> aluminum single crystals processed by severe plastic deformation, Mater. Charact. 75 (2013, Jan) 129–137, https://doi.org/10.1016/j.matchar.2012.10.008.
[28] I.L. Dillamore, H. Katoh, The Mechanisms of Recrystallization in Cubic Metals with Particular Reference to Their Orientation-Dependence, 2025.
[29] Q. Liu, C. Maurice, J. Driver, N. Hansen, Heterogeneous Microstructures and Microtextures in Cube-Oriented Al Crystals after Channel Die Compression, 1998.
[30] T. Kamijo, H. Adachihara, H. Fukutomi, Formation of a (001)[100] Deformation Structure in Aluminum Single Crystals of an s-Orientation, 1993.
[31] S. M'Guil, S. Ahzi, H. Youssef, M. Baniassadi, J.J. Gracio, A comparison of viscoplastic intermediate approaches for deformation texture evolution in face-centered cubic polycrystals, Acta Mater. 57 (8) (2009, May) 2496–2508, https://doi.org/10.1016/j.actamat.2009.02.001.
[32] M. Abadi, et al., TensorFlow: A System for Large-Scale Machine Learning [Online]. Available, http://arxiv.org/abs/1605.08695, 2016, May.
[33] Y. Lecun, Y. Bengio, G. Hinton, Deep learning, Nat. Publ. Group (2015, May 27), https://doi.org/10.1038/nature14539.
[34] I.N.D. Silva, Artificial Neural Networks: A Practical Course, Springer, Cham, Switzerland, 2017.
[35] D.P. Kingma, J. Ba, Adam: A Method for Stochastic Optimization [Online]. Available, http://arxiv.org/abs/1412.6980, 2014, Dec.